DEFECTS AND UNDULATION IN LAYERED LIQUID CRYSTALS

T. ISHIKAWA AND O. D. LAVRENTOVICH

Liquid Crystal Institute and Chemical Physics Interdisciplinary Program, Kent State University
Kent, OH 44242, U.S.A.

Abstract. Many systems, such as lamellar liquid crystals, block copolymers, ferrofluids and ferromagnets posses a one-dimensional periodic order. Cholesteric liquid crystals with large periodicity (say, 10 microns) represent a model system that allows one to directly determine layer configurations under a polarizing microscope and thus to study various elastic phenomena. We review recent studies of the so-called cholesteric "fingerprint textures" as an experimental model of two elastic effects: (1) distortions of the order parameter around an elementary edge dislocation and (2) undulations of layers in the magnetic field. Elastic distortions caused by the edge dislocation can be properly described only when the elastic free energy is supplemented by a non-linear term. Fitting the dislocation profile allows one to measure the penetration length of the system. With the known penetration length, one can verify the scenario of layers undulations in the magnetic field. The experiments reveal that the displacement of layers above the undulations threshold is much larger than the one expected from the Helfrich-Hurault theory which assumes that the boundaries impose infinitely strong surface anchoring. A revised theory that accounts for a finite surface anchoring for a bounded lamellar system fits the experimental data well. The feature of finite surface anchoring allows one to find an analytical description of undulations well above the threshold field, namely, the transformation of sinusoidal layer distortions into the saw-tooth distortions and reorientation of layers at the bounding substrates at very high fields.

O.D. Lavrentovich et al. (eds.),
Defects in Liquid Crystals: Computer Simulations, Theory and Experiments, 271–301.

1. Introduction

Various condensed matter phases show layered structure with a one dimensional (1D) periodicity. The best known example is the smectic A (SmA) liquid crystal, in which the translational symmetry is broken along one spatial direction by periodic modulation of the mass density. The centers of mass of elongated molecules are assembled in planes while the long axes of the molecules are on average perpendicular to these planes. An ideal distortion-free SmA can be imagined as a 1D stack of parallel planes separated by a constant distance d_0. In usual thermotropic SmA materials, d_0 is of the order of (1-10) nm and corresponds to the phase shift 2π of the density wave. According to the Landau–Peierls argument [1, 2], the amplitude of layer fluctuations in the 1D stack diverges in the thermodynamic limit; therefore, there is no true long-range 1D periodic order. Fortunately, the growth of fluctuations with the system size is slow, and for samples of realistic thicknesses (say, less than $10^6 d_0$), the fluctuative displacements are small as compared to d_0 (for numerical estimates, see, for example, [3]). The SmA is thus characterized by quasi-long-range order rather than true long-range order.

As a result of the peculiar order, both bulk (elastic) and surface properties of 1D-ordered materials are quite different from those of true 3D crystals. In what follows, we give a brief review of recent studies of two basic elastic phenomena in 1D-periodic systems: (a) layers distortions associated with an elementary edge dislocation and (b) development of layer distortions during the so-called Helfrich-Hurault undulations [4] in a confined cells with layers initially parallel to flat bounding plates. The undulations result from the competition between mechanical stresses or an applied external field that tends to orient the layers along the normal to the plates, on one hand, and the surface forces that tend to keep the layers parallel to the plates, on the other. The studies demonstrate importance of the non-linear elastic term in the elastic free energy density and the role of finite surface anchoring at the boundaries of a 1D-periodic system. The structure of the review is as follows.

The next Section 2 is of an introductory character. We first review the elastic theory of 1D-ordered phases that neglects the details of the inner structure of the layers (such as possible tilt of the molecules within the SmA layers). We describe the model system used in our studies, a cholesteric liquid crystal. The cholesteric liquid crystal has a periodicity in the range accessible for direct optical observations (tens of microns) and is confined in flat cells of approximately the same thickness; in effect, one deals with a 1D-periodic structure with distortions allowed in a 2D plane. Lubensky-de Gennes coarse-grained model describes the deformed cholesteric state

within the framework of the elastic theory developed for the SmA phase. We also recall some results on surface properties of layered systems, collected mostly for the traditional thermotropic SmA phases. Section 3 describe theory and experiments on edge dislocations. The dislocation profile cannot be described properly without the non-linear term in the elastic free energy. The experiment on the dislocation profile allows one to determine the important "elastic" or penetration length λ of the lamellar material. Section 4 describes undulation phenomena in the lamellar phase, in which the non-linear term plays an important role. We briefly review the standard Helfrich-Hurault model of undulations and then compare it to the experimental findings in the cholesteric periodic structure. The penetration length determined in the experiment on dislocation serves as a fitting parameter. We find that the layer displacements are much larger than what the standard theory predicts. The discrepancies are caused by finite surface anchoring of layers at the boundaries of the cell. A modified theoretical model that takes into account the finite surface anchoring fits the experimental data well. Finally, we briefly describe the behavior of undulating layers in a very strong field. The idea of finite anchoring allows one to get a better insight into the structural distortions in this regime.

2. Bulk Elastic and Surface Properties of Lamellar Systems

Elastic deformations in the system of layers are of the two types: (a) curvatures that leave the interlayer separation constant; the geometrical quantities of interest are the mean curvature and the Gaussian curvature of layers, Fig.1a; (b) dilations/compressions of layers, i.e., changes in d_0, Fig.1b. The corresponding free energy density that describes large bendings of layers and small dilations/compressions, is usually written in the form (see, e.g., [5])

$$f = \frac{1}{2}K\left(\frac{1}{R_1}+\frac{1}{R_2}\right)^2 + \overline{K}\frac{1}{R_1 R_2} + \frac{1}{2}B\gamma^2, \qquad (1)$$

where K is the splay elastic constant, $\overline{K}$ is the saddle-splay elastic constant, R_1 and R_2 are the principal radii of curvature, B is the Young (or compressibility) modulus for the 1D stack of layers, and $\gamma = (d-d_0)/d_0$ is the relative difference in the actual (d) and equilibrium non-perturbed (d_0) interlayer separation. Using the classical results from the theory of surfaces (see, for example, [6]), the splay and the saddle-splay curvature terms in Eq.(1) can be re-expressed through the director field $\mathbf{n}(\mathbf{r})$, defined as a unit normal to the layers:

$$\mathrm{div}\,\mathbf{n} = \pm\left(\frac{1}{R_1}+\frac{1}{R_2}\right);\ \frac{1}{2}\mathrm{div}\left(\mathbf{n}\,\mathrm{div}\mathbf{n} + \mathbf{n}\times\mathrm{curl}\,\mathbf{n}\right) = \frac{1}{R_1 R_2}. \qquad (2)$$

The mean-curvature term is related to the divergence of the director field. The saddle-splay term is of no importance in 2D geometries, since one of the principal radii of curvature is infinity. In 3D, because of its divergence nature, the saddle-splay term can be dropped when one is interested in smooth deformations that do not change the topology of layers. Transition from the flat layers to the weakly undulating layers is an example in which the saddle-splay term plays no role. We will not consider this term in what follows. Note finally that Eq.(1) assumes that the inner structure of layers does not change under deformations; for example, in the SmA phase, the molecules remain perpendicular to the layers.

2.1. WEAKLY DISTORTED SMECTIC A PHASE IN TWO DIMENSIONS

In many situations of practical interest, the departures of layers from an ideal equilibrium flat configuration are small and the expression for the elastic free energy density (1) can be simplified. We follow [5].

First of all, it is convenient to introduce a single scalar variable u, that describes the layer displacement field. If we choose the layers being perpendicular to the z-axis, then a layer located initially at coordinate z_0, is shifted to a new position $z = z_0 + u(x, z)$ as the result of the deformation. The equation of the deformed layer can be written as

$$z_0 = z - u(x, z). \tag{3}$$

The unit normal to the layers $\mathbf{n}$, is expressed through the displacement field as $\mathbf{n} = \pm\frac{\nabla[\mathbf{z}-\mathbf{u}(\mathbf{x},\mathbf{z})]}{|\nabla[\mathbf{z}-\mathbf{u}(\mathbf{x},\mathbf{z})]|}$, or, by expanding in series and retaining terms up to the second order, as

$$\mathbf{n} = \pm\left\{-\frac{\partial \mathbf{u}}{\partial \mathbf{x}}\left(\mathbf{1}+\frac{\partial \mathbf{u}}{\partial \mathbf{z}}\right), \mathbf{1}-\frac{\mathbf{1}}{\mathbf{2}}\left(\frac{\partial \mathbf{u}}{\partial \mathbf{x}}\right)^{\mathbf{2}}\right\}, \tag{4}$$

which allows one to rewrite the splay term as $\frac{1}{2}K\,(div\mathbf{n})^2 = \frac{1}{2}K\left(\frac{\partial^2 u}{\partial x^2}\right)^2$, Fig.1a. Let us now express γ through the displacement field: $\gamma = \frac{d-d_0}{d_0} = -1 + \frac{1}{|\nabla z_0|} \approx -1 + \frac{1}{n_z - \mathbf{n}\cdot\nabla\mathbf{u}}$, or

$$\gamma = \frac{\partial u}{\partial z} - \frac{1}{2}\left(\frac{\partial u}{\partial x}\right)^2. \tag{5}$$

The first-order derivative $\partial u/\partial z$ corresponds to compression or dilation of layers, Fig.1b. Standing alone, it would have a contribution $\left[\frac{\partial u}{\partial z}\right]^2$ to the energy density, in analogy to the Hooke's law. The derivative in the horizontal directions $\partial u/\partial x$ describes uniform rotation of the layers, Fig.1c.

The correction $\left[-\frac{1}{2}\left(\frac{\partial u}{\partial x}\right)^2\right]$ makes the compressibility term invariant with respect to uniform rotations. By symmetry, a uniform rotation of layers, say by an angle $\theta = \partial u/\partial x$, should not change the energy. However, it leads to a change in an effective layer spacing measured along the fixed vertical axis, $d \to d/\cos\theta$. The effective strain is $d\,(1 - 1/\cos\theta)\,/d \approx -\theta^2/2$ for a small θ. Therefore the invariant form of the compression term is $\frac{1}{2}B\left[\frac{\partial u}{\partial z} - \frac{1}{2}\left(\frac{\partial u}{\partial x}\right)^2\right]^2$ and the free energy density reads:

$$f = \frac{1}{2}K\left(\frac{\partial^2 u}{\partial x^2}\right)^2 + \frac{1}{2}B\left[\frac{\partial u}{\partial z} - \frac{1}{2}\left(\frac{\partial u}{\partial x}\right)^2\right]^2. \qquad (6)$$

The ratio of the two elastic moduli defines an important length scale $\lambda = \sqrt{K/B}$, called the "penetration length." Far below the SmA-nematic transition point, λ is of the order of interlamellar spacing. It is worth mentioning the effect of fluctuations-induced renormalization of the elastic constants in Eq.(6), predicted by Grinstein and Pelcovits [7]: at sufficiently long wavelengths, B decreases to zero and K logarithmically increases to infinity. However, the changes are rather small, a few percent at the scales of 100 microns for typical SmA materials [7].

The term $\frac{1}{2}\left(\frac{\partial u}{\partial x}\right)^2$ in Eq.(6) makes the theory nonlinear and complicates analytical calculations. In some cases, it is possible to assume that $\frac{(\partial u/\partial x)^2}{|\partial u/\partial z|} \ll 1$, and consider only the linear model with the compressibility term $\frac{1}{2}B\left(\frac{\partial u}{\partial z}\right)^2$. One example, as we shall see below, is a dislocation profile in a material where the penetration length is much larger than the Burgers vector of the dislocation [8]. However, in most cases, the simplification cannot be justified. For example, the behavior of layers above the threshold of the Helfrich-Hurault undulation can be calculated only when the non-linear term is retained.

2.2. LUBENSKY-DE GENNES COARSE-GRAINED MODEL OF THE CHOLESTERIC PHASE

Elastic properties of the lamellar systems were studied mostly for the conventional smectic phases. Their interlayer spacing is usually small, few nanometers in the majority of thermotropic and surfactant-based lyotropic smectic materials. There are some remarkable but rare exceptions in the dilute lyotropic systems with the period reaching 10-100 nm, see, for example, [9] and references therein. At these scales, it is hard to visualize the behavior and geometry of layers directly, say, under the polarizing microscope. Fortunately, there are many other systems, such as cholesteric

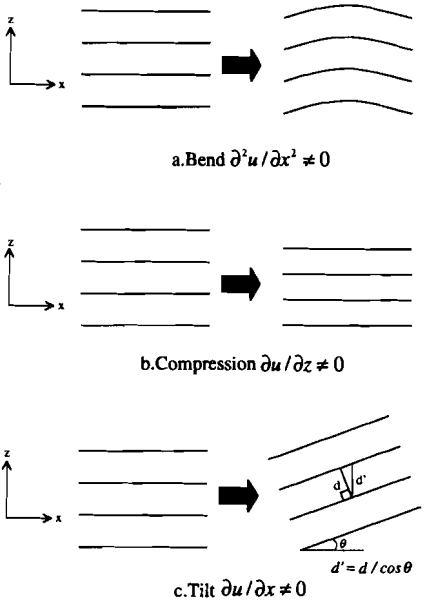

Figure 1. Various modes of deformation in a 1D lamellar system.

liquid crystals, that have a period in the range of microns (easily accessible for direct polarizing microscopy observations) and exhibit elastic properties close to that of smectic phases [10]. Note that unlike the smectic phases, the cholesteric phase does not have a periodic modulation of density: it is the orientation of the director that changes in the space, at the background of a constant mass density.

The cholesteric phase is formed by chiral molecules (or chiral dopants to the nematic host) and is characterized by a unidirectionally twisted director (unbounded sample). The cholesteric pitch P_0, the length over which the director rotates by 2π, is usually in the range of 0.1-100 microns. According to the coarse-grained elastic model proposed independently by Lubensky [11] and de Gennes [10], when the scale of deformations (a radius of curvature) is much larger than P_0, elastic properties of the cholesteric phase are close to that of smectic phase outlined above (see also [12]). The coarse-grained theory operates with the displacement field $u(x, z)$. The rotation-invariant free energy density for cholesteric deformations restricted to a 2D plane (x, z) which is parallel to the cholesteric axis $\widehat{m}$ is exactly of the same form as the expression (6) above. The difference is only in the meaning of the elastic constants B and K. The two constants can be related to the Frank constants of twist (K_2) and bend (K_3) in the Frank-Oseen elastic energy

density, traditionally used for the description of nematic and large-pitch cholesteric phases [10]. Compression of the cholesteric structure changes the pitch, thus for an ideal stack of flat layers compressed or dilated along the helical axis, the correspondence is $B = K_2 q_0^2$ where $q_0 = 2\pi/P_0$. The bending of layers is the splay deformation of the cholesteric axis $\widehat{m}$. The effective value of K has been calculated by considering an ideal cylindrical configuration of the cholesteric layers; it follows that $K = 3K_3/8$. Of course, the relationships between the pairs (K, B) and (K_2, K_3) would be different from the formulas above when the cholesteric is confined between two glass plates since the surface anchoring would modify the ideal helicoidal cholesteric twist. Nevertheless, it is interesting to note that the penetration length given by $\lambda = \frac{P_0}{2\pi}\sqrt{\frac{3K_3}{8K_2}}$ in this idealized model is noticeably smaller than $P_0/2$, the period of an ideal unperturbed cholesteric helix. For example, with a typical $K_2 = 0.5K_3$, one obtains $\lambda = 0.34\,(P_0/2)$. In the realistic case of bounded and distorted cholesteric, λ is the subject of experimental determination; note also that the true periodicity of a bounded cholesteric might be closer to P_0 rather than to $P_0/2$, as discussed in section 3.2.

2.3. SURFACE ANCHORING

The preferred orientation at the SmA boundary is most often "homeotropic", with the director perpendicular to the surface, or "tangential", with the director in the plane of the boundary, see, e.g., [13]. A rare case of tilted equilibrium anchoring has been reported for lyotropic biphasic systems, for the interface between the lamellar and sponge domains [14, 15].

Historically, two different parameters have been used to characterize the anisotropy of the interfacial energy for SmA: (a) the "anchoring coefficient" W_a similar to its counterpart in the nematic phase, and (b) anisotropy of the surface energy, defined through the difference in the surface energy for tangential and normal anchoring, $\Delta\sigma = \sigma_{||} - \sigma_{\perp}$. To illustrate the difference between the two, we will assume that the homeotropic orientation corresponds to the minimum of the surface energy density.

The anchoring coefficient W_a is introduced to describe small deviations from the equilibrium "easy axis" of surface orientation, through the formula that relates the work (per unit area) needed to deviate the director, to the angular amplitude θ of this deviation; θ is measured from the normal to the interface and is also equal to the angle between the layers and the substrate. In nematics, an approximate expression is of the form $W(\theta) = \frac{1}{2}W_a\theta^2$. In SmA, such an approximation might be valid only in some special cases, for example, when the surface layers periodically undulate. When the layers tilt is uniform along the boundary, it is more appropriate to expect that some of the smectic layers are terminated by dislocations, as in the model of tilted

grain boundaries in solid crystals, see, for example, [16]. The anchoring energy would be then proportional to the number of dislocations (assuming that the latter are well separated and do not interact for very small θs), i.e, it would be linear in θ : $W(\theta) = W_a|\theta|$. The coefficient W_a is expected to be much larger in the SmA phase than in the corresponding nematic phase, above the SmA-nematic transition, as the layered structure is incompatible with tilted alignment at the surface [17, 18]. Experimentally, W_a was found to change with temperature within the range $W_a \approx (0.3 - 30) \times 10^{-3} J/m^2$ for the thermotropic SmA material (4'-trans-butyl-4-cyano-4-trans-heptyl-1,1'-bicyclohexane, E.M. Industries) [18]. The last result leads to the estimate $W_a \approx Bd_0$ [18]. A similar estimate $W_a \approx Kq_0$ emerges as the coefficient of the "intrinsic"polar anchoring in the cholesteric phase, related to the fact that uniform tilted orientation of the "easy axis" at the substrate is incompatible with the periodic cholesteric twist (=layered structure) [19]. In the nematic phase, this "intrinsic" layers-related anchoring is absent, and the polar anchoring coefficient W_a is usually few orders of magnitude smaller than $W_a \approx Bd_0$ in the SmA phase, see, for example [13].

The anisotropy $\Delta\sigma$ of the surface energy is introduced in a different context of large departures from the easy axis. These large departures are observed in textures with focal conic domains (FCDs) based on confocal pairs of ellipse and hyperbola, or, in the simplest case, a circle and a straight line, see Fig.2. As seen in Fig.2, when the circular FCD base is located at the interface, the layers are perpendicular to the bounding surface inside the domain and parallel to the surface outside the domain. Each time a circular FCD is introduced into the system, it changes the surface energy by $\sim r^2\Delta\sigma$ and the elastic energy by $\sim Kr$, where r is the radius of the base. If $\sigma_{||} < \sigma_{\perp}$, the process is energetically favorable, as long as the domain is large enough, i.e. larger than the critical size $r^* \sim K/(-\Delta\sigma)$ [20]. Thus the FCDs serve as "facets" in bounded smectic samples when the interface favors tangential anchoring of the molecules. The feature is clearly visible in the SmA nuclei emerging from the isotropic melt [21] or in SmA droplets suspended in isotropic fluids [20]. For a SmA-isotropic melt interface [21] and for the SmA - glycerin interface, experiments yield $r^* \sim K/(-\Delta\sigma) \sim 1\mu m$ or less, so that $|\Delta\sigma| \geq 10^{-5} J/m^2$ [20] . Therefore, $|\Delta\sigma|$ might be smaller than W_a. The reason is a non-monotonous character of the surface energy $W(\theta)$ with two minima at $\theta = 0$ and $\theta = \pi/2$ and a relatively high maximum at intermediate values of θ that corresponds to strong distortions of layers near the surface, see [17] for more details.

3. Edge Dislocations

Elementary topological defects in systems with broken translational symmetry are dislocations. Dislocations have been an object of intensive studies

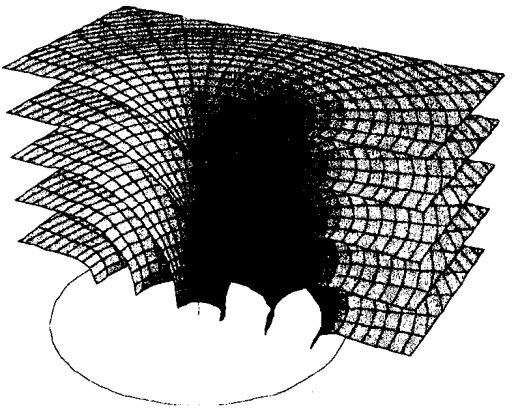

Figure 2. A circular focal conic domain with a pair of defect lines: a circle located at an interface and a straight line passing through the center of the circle.

mainly in solids with 3D periodicity [22]. There are substantial differences between these classic dislocations and dislocations in media with reduced dimensionality of order, such as smectic, cholesteric, or hexagonal phases in liquid crystalline, polymer and other soft-matter systems. These differences manifest themselves in dislocation profiles (configurations of the order parameter associated with the defect), dislocation self-energy and interaction energy, see the book by Kleman [23] and the review by Holyst and Oswald [24]. Calculation of properties of dislocation lines is a classic problem of the elastic theory.

For an edge dislocation in a 1D smectic system, the first solution has been suggested by de Gennes [25] within the framework of a linear theory, see also [23].

3.1. LINEAR THEORY

In the linear approximation for the free energy density (6), in which the compressibility term is just $\frac{1}{2}B\left(\frac{\partial u}{\partial z}\right)^2$, the corresponding Euler-Lagrange equation is

$$\lambda^2 \frac{\partial^4 u}{\partial x^4} - \frac{\partial^2 u}{\partial z^2} = 0. \tag{7}$$

Let the edge dislocation of the Burgers vector $(0, b)$ be centered at $(x, z) = (0, 0)$. The solution that satisfies the boundary conditions $u\,(x < 0, z = +0) = 0$ and $u\,(x > 0, z = +0) = b/2$ (we consider the upper half-plane only,

thanks to the symmetry $u(z) = -u(-z)$) is

$$u(x,z) = \frac{b}{4} + \frac{b}{4\pi}\int_{-\infty}^{+\infty} \frac{dq}{iq} e^{iqx-\lambda q^2 z}. \tag{8}$$

or, in other notations,

$$u(x,z) = \frac{b}{4\sqrt{\pi}}\int_{-\infty}^{x/\sqrt{\lambda z}} e^{-t^2/4}dt = \frac{b}{4}\left\{1 + erf\left(\frac{x}{2\sqrt{\lambda z}}\right)\right\}. \tag{9}$$

where $erf(...)$ is the error function defined as $erf(\eta) = \frac{2}{\sqrt{\pi}}\int_0^\eta e^{-t^2}dt$. The tilt of the layers around the dislocation,

$$\theta(x,z) = \frac{\partial u}{\partial x} = \frac{b}{4\sqrt{\pi z\lambda}} \exp\left(-\frac{x^2}{4z\lambda}\right) \tag{10}$$

is significantly different from zero only inside the parabola $x^2 = 4z\lambda$; it decreases slowly with z on a typical distance $\frac{x^2}{4\lambda}$, and decreases rapidly with x inside the parabola [10]. The inflection points of the curved layers, where $\frac{\partial^2 u}{\partial x^2} = 0$, are located exactly at the $z-$axis ($x = 0$).

The above calculations, Eq.(7)-(10), are valid if $\frac{(\partial u/\partial x)^2}{|\partial u/\partial z|} \ll 1$. Within the parabola $x^2 = 4z\lambda$, the ratio $\frac{(\partial u/\partial x)^2}{|\partial u/\partial z|}$ is roughly equal to b/λ, and is independent of z. Therefore, the linear theory is justified only for the materials with $b << \lambda$. If the last condition does not hold, one should consider the more general non-linear theory of Brener and Marchenko, see [8] and the next section 3.2.

Experimental quantitative verifications of the edge dislocation profile are scarce. Maalorum et al. [26] used atomic force scanning microscopy to study the free surface profile of a smectic copolymer domain deposited onto a silicon wafer surface. Later, they developed a theory [27] to explain the observed profile by the surface-tension effects. However, to our knowledge, there is no experimental study on the dislocation profile in the bulk of a layered system [28].

As pointed above, the linear theory is valid only for materials that satisfy the rather restrictive condition $b << \lambda$. Clearly, the smallest Burgers vector is that of an elementary dislocation with b equal to the period of the structure. At the very same time, dimensional considerations suggest that λ should be close in the order of magnitude to d_0. Therefore, the condition $b << \lambda$ does not seem to hold in the majority of situations. For example, it is not expected to hold in the cholesteric structures, where λ is supposed to be smaller than $P_0/2$. Therefore, the cholesteric structures might be an excellent example of a markedly "non-linear" system. Below we describe

experimental results on layers profile for an edge dislocation in the so-called "fingerprint" texture of a cholesteric liquid crystal.

3.2. EXPERIMENTAL DISLOCATION PROFILE AND NON-LINEAR THEORY.

As the system to study, we have chosen a cholesteric "fingerprint" texture with a period $w \sim 10$ μm [29]. The fingerprint texture occurs when the cholesteric material is sandwiched between two flat glass plates that tend to align the helicoid axis in the plane of the cell. When viewed from above in polarized light, the periodic director distortions in the (x, z) plane of the cell result in a fingerprint-like texture. To avoid any in-plane torques in the sample, we coated the glass plates with an alignment layer (polyimide JALS 214 from JSR Inc., Japan) that orients the director perpendicularly to the plates. As a result, even when the external field is absent, surface anchoring greatly modifies the ideal cholesteric helicoid. First of all, the helix is somewhat unwind by surface anchoring at the glass plates. Second, the surface anchoring breaks the symmetry of the structure, making the period close to P_0 rather than to $P_0/2$, i.e., $w \geq P_0$, see [30] and the chapter by Shiyanovskii et al. in this book.

Mylar films were used as spacers setting the cell thickness $l = 14$ μm. Nematic liquid crystal 5CB was mixed with the chiral dopant CB15 to adjust the pitch P_0 to 14μm so that $l/P_0 \sim 1$. When the cell is filled with the cholesteric mixture, a fingerprint texture occurs with characteristic "stripes" oriented randomly in the plane of the cell. To align the stripes along one direction, the texture in the cell was relaxed in the magnetic field till only a few well-separated (1 cm) dislocations were left in the system. The magnetic field was then switched off. The size of the cell was large (2.5 cm x 2.5 cm) as compared to the stripe periodicity to reduce the edge effects and to mimic the 'bulk' behavior of dislocations. We have observed only elementary dislocations with the Burgers vector $b = w \approx 15$ μm. An example of an isolated elementary edge dislocation is shown in Fig.3.

Large period of the cholesteric structure allows for direct experimental determination of the displacement field $u(x, z)$. The accuracy is about 0.4 μm, determined mainly by the microscope's resolution. The location of the dislocation $(x, z) = (0, 0)$ was set at the tip of the semicircular end of the inserted layer, Fig. 3b.

The layers profile of the edge dislocation does not fit the classical linear elastic theory, Fig.4. Namely, the inflection points of the layers are shifted away from the center line $x = 0$, towards the part $x < 0$ with smaller number of layers, in accordance with the qualitative predictions of Brener and Marchenko [8] and Kleman [31] for systems with a small penetration length, $\lambda < w$. The shift is visible not only near the core of the dislocation;

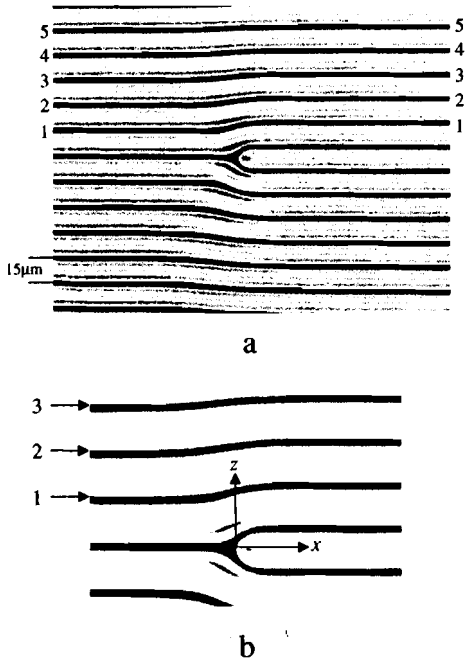

Figure 3. (a) A typical isolated elementary edge dislocation in a well-aligned cholesteric fingerprint texture. (b) Coordinate frame for profile measurement. Redrawn from [29].

in fact, it increases for the layers located further away from the core. Therefore, in order to describe the dislocation profile, one has to resort to the more general non-linear analysis [8] with the elastic energy density given by Eq.(6). The model leads to the following dislocation profile [8]:

$$\begin{aligned} u(x,z) &= 2\lambda \ln\left[1 + \frac{e^{b/4\lambda}-1}{2\sqrt{\pi}} \int_{-\infty}^{x/\sqrt{\lambda z}} e^{-t^{2/4}} dt\right] \\ &= 2\lambda \ln\left[1 + \frac{e^{b/4\lambda}-1}{2}\left\{1 + erf\left(\frac{x}{2\sqrt{\lambda z}}\right)\right\}\right], \end{aligned} \tag{11}$$

where $erf(...)$ is the error function defined above. In the limit $b << \lambda$, Eq.(11) reduces to the result from the linear elastic theory [10, 23] and Eq.(9).

Figure 5 illustrates the basic features of the nonlinear solution, Eq.(11) as a function of the ratio $b/\lambda = 0.2$; 1; 10 and 100. We deliberately exaggerate the plausible range of the values b/λ to highlight the qualitative features of the dislocation profiles. All figures show a half of the (x, z) plane, with $z > 0$. We remind that the linear limit is achieved at $b/\lambda \to 0$, i.e.,

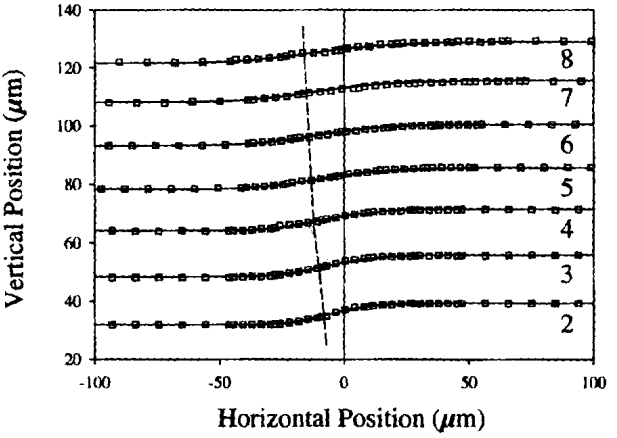

Figure 4. Experimentally obtained profiles for the second through the eighth layers around an elementary edge dislocation. The data are fitted with the nonlinear theory, Eq.(11). Experimental inflection points are marked by the dashed line. Redrawn from [29].

the plots labelled "$b/\lambda = 0.2$" are the closest to the linear behavior. Part (a) of Fig.5 shows the geometry of layers. Part (b) represents the contour plots of the layers tilt $\partial u/\partial x$. Part (c) shows the dilations/compressions $\left[\frac{\partial u}{\partial z} - \frac{1}{2}\left(\frac{\partial u}{\partial x}\right)^2\right]$ of the layers, or, equivalently, the quantity $\lambda\partial^2 u/\partial x^2$ related to the curvature. Note that according to Eq.(9) and Eq.(11), the (dilation/curvature) ratio, defined as $\left(\frac{\partial u}{\partial z}\right) / \left(\frac{\partial^2 u}{\partial x^2}\right)$ in the linear theory and $\left[\frac{\partial u}{\partial z} - \frac{1}{2}\left(\frac{\partial u}{\partial x}\right)^2\right] / \left(\frac{\partial^2 u}{\partial x^2}\right)$ in the non-linear theory of dislocation, equals λ in both cases.

As seen in Fig.5, the main difference between the linear and nonlinear models is the asymmetry of the dislocation profile. In the linear theory, Eq.(9), the change in the displacement field mainly takes place in the range $-\sqrt{\lambda z} < x < \sqrt{\lambda z}$ and the points of inflection are located at $x = 0$. The nonlinear theory (11) predicts that the inflection points are located at $x < 0$. The displacement changes mainly in the region of negative x, with the lower boundary being $|x_{\min}| \sim \sqrt{bz} > \sqrt{\lambda z}$ [8]. This results in the effective shift of the displacement profile to the negative x's. If the ratio b/λ becomes very large, the dislocation profile transforms dramatically, see the plots labeled "$b/\lambda = 100$" in Fig.5. The structure of the dislocation becomes more and more similar to the model of a dislocation with a core that splits

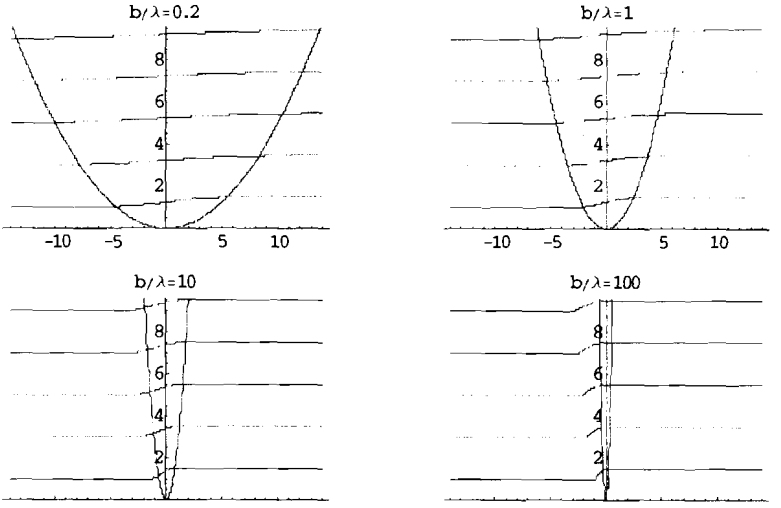
b/λ=0.2
b/λ=1
b/λ=10
b/λ=100
8
6
4
2
-10
-5
5
10

(a)

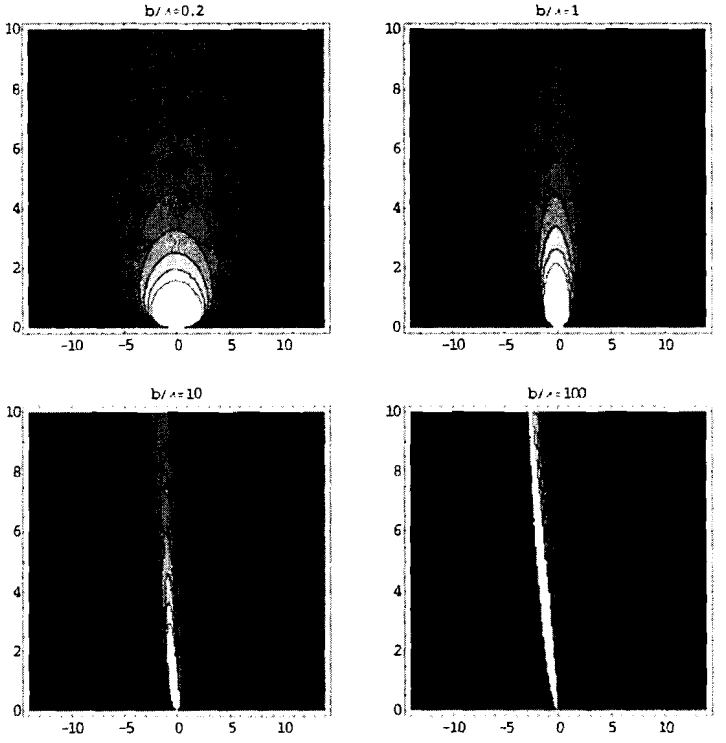
b/λ=0.2
b/λ=1
b/λ=10
b/λ=100
10
8
6
4
2
0
-10
-5
0
5
10

(b)

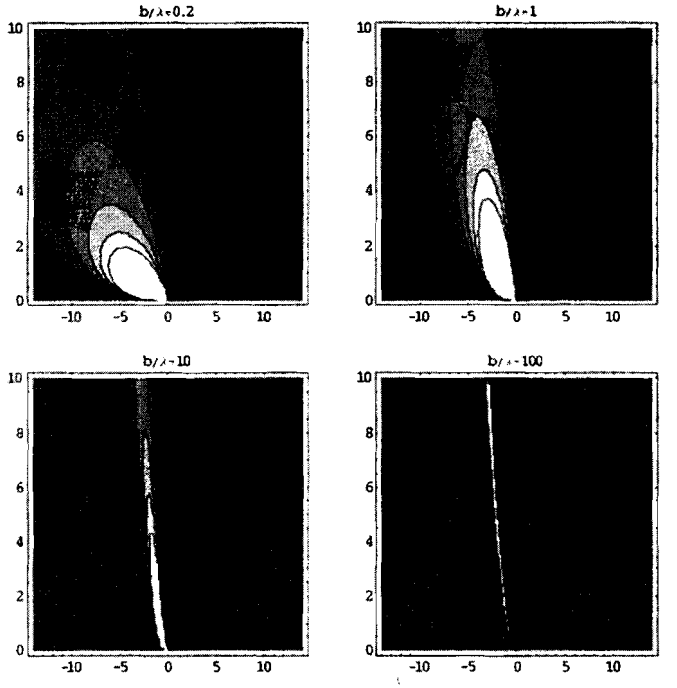

(c)

Figure 5. Properties of the edge dislocation according to the nonlinear Brener-Marchenko model Eq.(11), as a function of the ratio b/λ: (a) layers profile; (b) contour plots of layers tilt $\partial u/\partial x$; (c) dilations/compressions $\left[\frac{\partial u}{\partial z} - \frac{1}{2}\left(\frac{\partial u}{\partial x}\right)^2\right]$ of the layers, or, equivalently, the curvature-related quantity $\lambda\partial^2 u/\partial x^2$.

into a pair of disclinations, see Fig.6. The later structure has been proposed as an alternative model of a dislocation with a large Burgers vector, see [32] and [23].

We now return to the discussion of the actual experimental profile. Figure 4 shows the experimentally measured displacements of the second through the eighth layers around the dislocation core. The displacement field was determined at a sharp border line between the dark and bright parts of the texture, indicated by arrows in Fig.3b. The first layer, which is too close to the core region, is disregarded. Evidently, the nonlinear model fits the experimental data much better than the linear model. Moreover, the nonlinear theory fits the whole set of seven layers presented in Fig.4 with the very same pair of parameters: $b = 14.9\mu$m and $\lambda = 2.65\mu$m. Note that the attempts to fit the data with the linear theory by shifting the layers do not allow to fit all the layers simultaneously, see [29] for more details. Therefore, the observed asymmetry in the displacement field is a

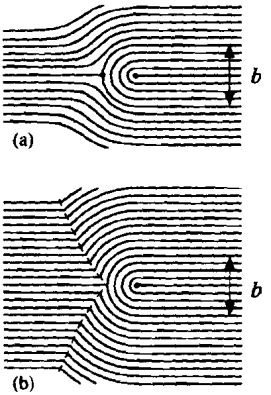

Figure 6. An edge dislocation of a large Burgers vector split into a pair of two disclinations (a) and a dislocation model with a vanishing λ; the layers are mostly curved, dilations are reduced at the expense of a parabolic singular wall (b). Redrawn from [5].

real manifestation of the nonlinear elastic effects rather than an artifact associated with the setting of the coordinate frame.

The outcome of the experiment above is not only the fitting of the dislocation profile with the non-linear theory, but also the experimental determination of the penetration length λ. In the next chapter, this method to determine λ will be used to verify the scenario of the undulation instability.

4. Layers undulations (Helfrich-Hurault instability)

An important feature of 1D lamellar systems (and 2D-positionally ordered columnar systems) is that the curvature deformations are capable of relaxing mechanical or field-induced stresses. The layers profile around an edge dislocation is one example. Another example is that of layer undulations.

Because of the material anisotropy, orientation of a layered system can be changed by external fields. For example, the magnetic field would orient the layers parallel or perpendicular to itself, depending on the sign of diamagnetic anisotropy. The free energy density of the system depends on the angle between the director and the magnetic field $\mathbf{H}$. In what follows, we consider the stack of layers originally perpendicular to the z-axis. The external field is directed along the very same z-axis, $\mathbf{H} = (\mathbf{0}, \mathbf{0}, \mathbf{H})$. The diamagnetic contribution to the free energy density is $-\frac{c}{2}H^2\left(\frac{\partial u}{\partial x}\right)^2$, where c describes the strength of coupling between the layers and the field. In the SmA phase, $c = -\chi_a$, where $\chi_a = \chi_{||} - \chi_{\perp}$; and $\chi_{||}$, $\chi_{\perp}$ are the magnetic susceptibilities along and perpendicular to the director, respectively (we use CGS units). Normally, in the SmA materials $\chi_a > 0$ and the external field directed along the z-axis would only stabilize the initial flat system

of layers. However, in cholesterics, the effective value of χ_a (referred to the helical axis rather than to the local director) is normally negative, which makes the field-induced undulations possible.

The total bulk free energy density of the 1D layered system in the external magnetic field thus reads [10]

$$f = \frac{1}{2}K\left(\frac{\partial^2 u}{\partial x^2}\right)^2 + \frac{1}{2}B\left[\frac{\partial u}{\partial z} - \frac{1}{2}\left(\frac{\partial u}{\partial x}\right)^2\right]^2 + \frac{\chi_a}{2}H^2\left(\frac{\partial u}{\partial x}\right)^2. \qquad (12)$$

The field-induced rotation of layers cannot be free if the system is bounded. The compromise between the surface and field action results in undulation of layers, also called the Helfrich-Hurault instability [4]. The field-induced phenomenon has a mechanical analog: undulations of layers can be caused by an imposed dilation [33]. In this case, the quantity $\chi_a H^2$ in the last formula Eq.(12) is replaced by $-B\left(a' - a\right)/a$ where $\left(a' - a\right)/a > 0$ is a relative dilation of the cell, see e.g., [34].

4.1. HELFRICH-HURAULT MODEL

Let us briefly review the standard analysis of Helfrich-Hurault undulations [4, 10], in the 2D geometry of (x, z) plane. The layers are confined between two parallel "surfaces" placed at a distance $a >> l$. We remind that l is the distance separating the glass plates, which does not enter explicitly the discussion of undulations in the (x, z) plane (this plane is parallel to the glass plates). The applied field $(0, 0, H)$ directed along the normal to the layers tends to orient them parallel to itself ($\chi_a < 0$), but this reorientation is opposed by surface forces that keep the layers at the boundaries immobilized, $u\left(z = -a/2\right) = u\left(z = a/2\right) = 0$, see Fig.7. The compromise is achieved by periodic undulation of layers that occur above some threshold field H_c. For a 2D system, the undulation pattern in the (x, z) plane is assumed to be of a form [4, 10]

$$u\left(x, z\right) = u_0 \cos q_z z \sin q_x x, \qquad (13)$$

where $q_z = \pi/a$; $z = 0$ corresponds to the center of the gap. To find the threshold field, one calculates the energy per one period of undulation from the energy density (12), retaining terms up to the order of u_0^2:

$$\tilde{f} = \frac{q_x}{2\pi}\int_{-a/2}^{a/2} dz \int_0^{2\pi/q_x} f dx = \frac{K}{8}\left\{\frac{\pi^2}{a\lambda^2} + q_x^4 a - \frac{a q_x^2}{\xi^2}\right\} u_0^2, \qquad (14)$$

where $\xi = \frac{1}{H}\sqrt{\frac{K}{|\chi_a|}}$ is the diamagnetic coherence length. Considering $\tilde{f}$ as a function of q_x with ξ as a parameter of a family of curves, the critical

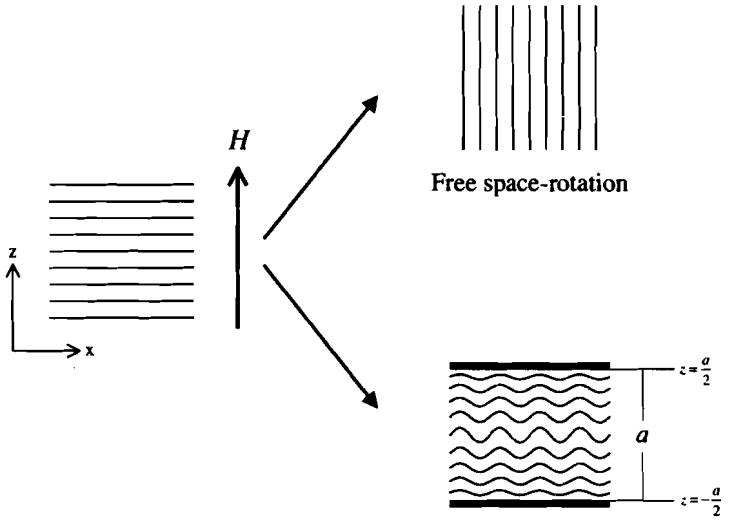

Figure 7. Scheme of layers response to the applied magnetic field. In free space, the layers rotate uniformly. In a bounded sample the layers undulate.

field is obtained from the condition that $\widetilde{f}(q_x, \xi)$ becomes tangent to the horizontal line for a particular $\xi = \xi_c$, Fig.8. At the minimum (q_x, ξ_c) of $\widetilde{f}$, one has the condition $q_x^2 = \frac{1}{2\xi^2}$ which yields the threshold field [4, 10]:

$$H_c = \sqrt{\frac{2\pi K}{\lambda a \left|\chi_a\right|}}. \tag{15}$$

The corresponding wavelength of undulations along the horizontal x-axis is given by $q_{xc}^2 = \frac{\pi}{a\lambda}$. The last formula is also valid for the dilation-induced undulation instability; it was used to determine the penetration length λ in thermotropic SmA by light scattering techniques, see [35] and references therein.

In order to derive the displacement of layers above the critical field, we need to take into account the higher order term in u_0, which means employing the non-linear theory, Eq.6. In vicinity of the transition,

$$\widetilde{f} = \left\{ \frac{\pi^2}{2a\lambda^2} - \frac{\pi}{4\xi^2\lambda} \right\} u_0^2 + \frac{9\pi^2}{256\lambda^4 a} u_0^4 = \frac{\pi}{4\lambda} \left\{ \frac{1}{\xi_c^2} - \frac{1}{\xi^2} \right\} u_0^2 + \frac{9\pi^2}{256\lambda^4 a} u_0^4. \tag{16}$$

In analogy with Landau theory of the second order phase transition, one obtains $u_0(H)$ immediately above the threshold by minimizing (16) with respect to u_0 [4, 10, 36]:

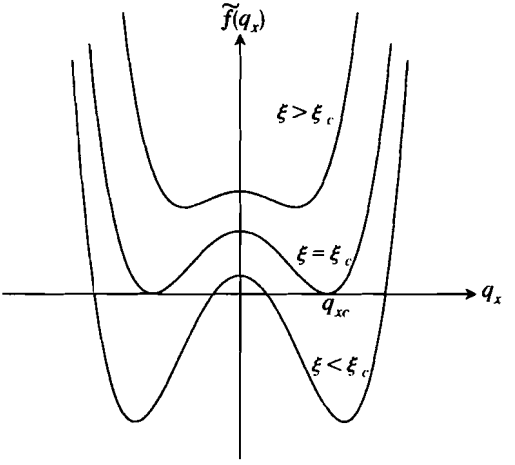

Figure 8. Plot of $\tilde{f}$ as a function of q_x, for various values of diamagnetic coherence length ξ, see Eq.(14). The critical field of Helfrich-Hurault instability is obtained when the curve $\tilde{f}(q_x, \xi)$ becomes tangent to the horizontal axis.

$$u_0 = \frac{8\lambda}{3}\left(\frac{H^2}{H_c^2} - 1\right)^{1/2}. \tag{17}$$

The simplicity of the expression above offers an opportunity either to verify the predictions of the Helfrich-Hurault model, if λ is known, or to use the model as an independent technique to determine the penetration length λ [36]. Although undulation instabilities have been observed for many 1D layered and 2D columnar systems, including smectic [33, 37], cholesteric [38] and columnar [39, 40] liquid crystals, magnetic stripe phases [41, 42], ferrofluids [43] and apparently block copolymers [44, 45], we are not aware of any experimental data that would verify the predictions of Eq.(17). Relevant experiments on the model cholesteric system will be described in the next section 4.2. We will take advantage of the fact that the penetration length λ can be measured in the independent experiments with the edge dislocation, section 3.2.

4.2. UNDULATIONS PROFILE NEAR THE THRESHOLD: EXPERIMENT

The model system with an undulating stripe pattern is created in two steps: (i) obtaining a uniform stripe texture in a cholesteric homeotropic cell similar to the experiment with the edge dislocation [29]; (ii) generation of undulations by a magnetic field applied in the plane of the cell. The magnetic field is applied in the direction z *perpendicular* to the cholesteric

stripes to cause undulations, see Fig. 9 and 10. Since the separation l between the glass plates is close to the pitch P, the system is quasi-2D and undulations occur only in the (x, z) plane parallel to the glass plates [46]. The mylar stripes serve as bounding walls.

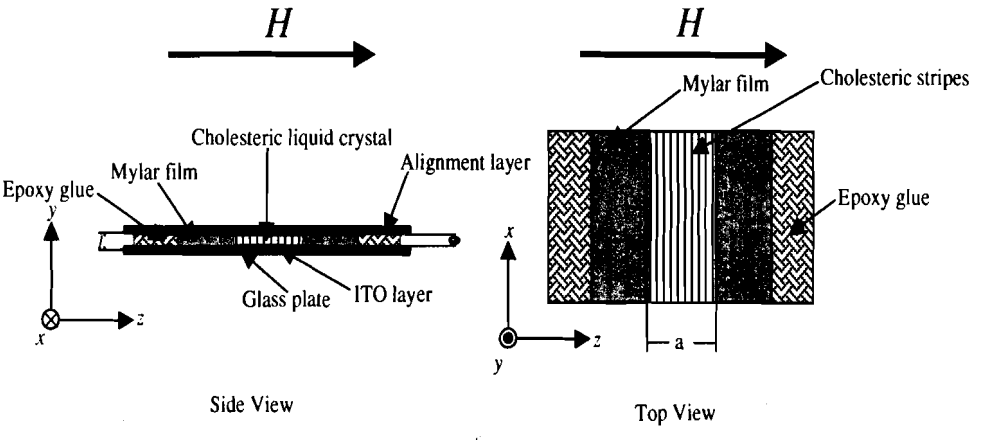

Figure 9. Geometry of the sample for the undulation experiment.

Figure 11 shows the field dependence of the displacement amplitude u_0 (along the z-axis) of the layer initially in the middle of the cell, $z = 0$. According to the classic theory, Eq.(17), valid just above the threshold field H_c, the function $u_0(H/H_c)$ depends only on one material parameter, namely, the penetration length $\lambda = \sqrt{K/B}$. The threshold field $H_c = \sqrt{\frac{2\pi K}{\lambda a|\chi_a|}}$ depends also on the diamagnetic anisotropy χ_a of the material. The experimental data $u_0(H/H_c)$ in Fig.11 can be approximated by Eq.(17) only when $\lambda = (8.5 \pm 1.7)$ μm. On the other hand, independent measurements of the penetration length from the dislocation profile in the cholesteric mixture under study yields a much smaller length, $\lambda = (2.9 \pm 0.1)$ μm; this λ is too small to allow Eq.(17) to describe the data in Fig.11. Thus the most plausible source of discrepancies between the experiment and the theory is the form of Eq.(17) itself.

Equation (17) was derived in the approximation that the layer displacement is strictly zero at the boundaries. Closer investigation of the undulation textures reveals that the displacement of the very first layer at the boundary is actually nonzero, Fig.12. In the next section we re-analyze the undulation instability by taking into account the finite surface anchoring at the bounding walls.

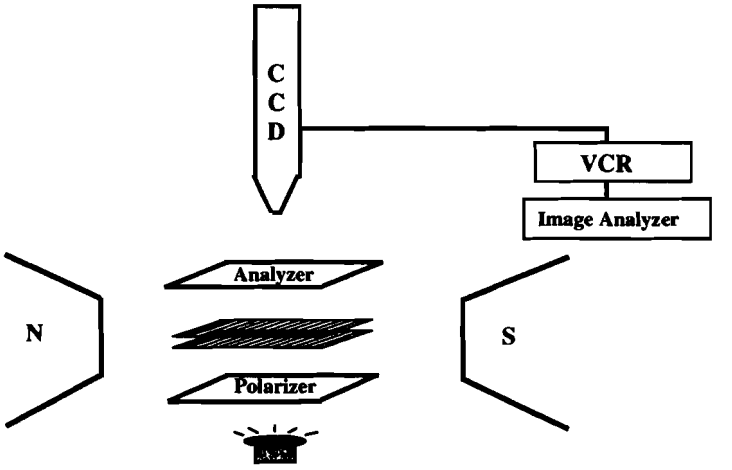

Figure 10. The experimental setup for polarizing-microscope observations of layers undulations in the magnetic field.

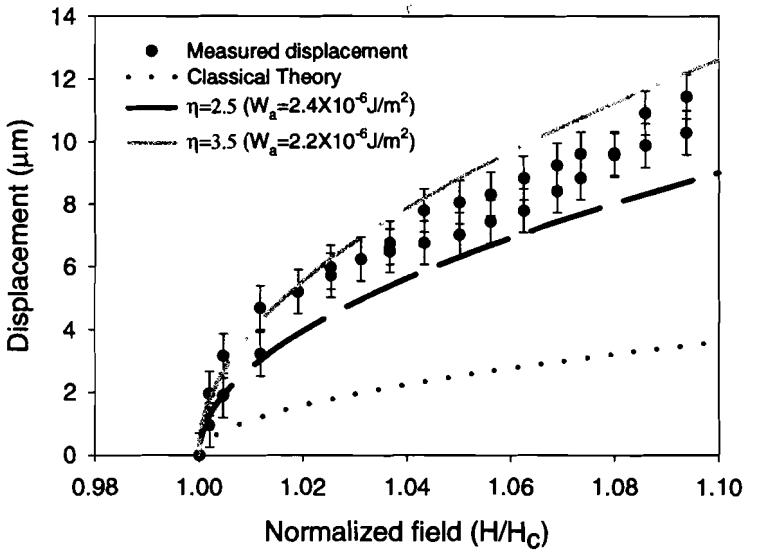

Figure 11. Comparison of the measured displacement amplitude with the theory. Dotted line shows u_0 predicted by the classical theory, Eq (17). The measured displacement falls between the two lines, Eq.(25) with $\eta = 2.5$ and 3.5. With the value $B = 0.44 J/m^3$ estimated from the coarse grained theory, the upper and the lower curves correspond to the anchoring coefficient $W_a = 2.2$ and $2.4 \times 10^{-6} J/m^2$, respectively.

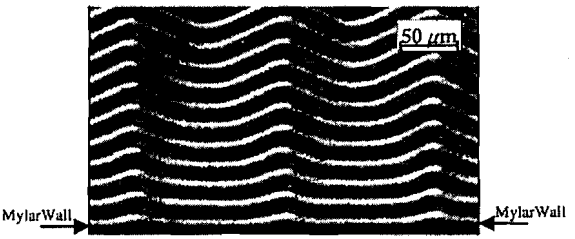

Figure 12. Undulation pattern near the mylar wall above the threshold field, $H = 1.05H_c$, where $H_c = 0.65T$.

4.3. UNDULATIONS IN A CELL WITH A FINITE ANCHORING

The free energy of the system, assumed periodically undulating along the x-direction, $u(x) \sim \sin q_x x$, is written (per one period $2\pi/q_x$) as

$$F = \int_0^{2\pi/q_x} dx \int_{-a/2}^{a/2} \frac{1}{2} dz \left\{ B\left[\frac{\partial u}{\partial z} - \frac{1}{2}\left(\frac{\partial u}{\partial x}\right)^2\right]^2 + K\left(\frac{\partial^2 u}{\partial x^2}\right)^2 + \chi_a H^2 \left(\frac{\partial u}{\partial x}\right)^2 \right\}$$
$$+ \frac{1}{2} W_a \int_0^{2\pi/q_x} dx \left[\left(\frac{\partial u}{\partial x}\right)^2_{z=-a/2} + \left(\frac{\partial u}{\partial x}\right)^2_{z=a/2} \right], \tag{18}$$

where the surface term with the anchoring coefficient W_a is taken proportional to $(\partial u/\partial x)^2$ [10]. It is a legitimate assumption since the tilt $\partial u/\partial x$ of layers is small and changes sign periodically along the x-axis. A coherent tilt with $\partial u/\partial x = const$ would require a lattice of dislocation and a surface term $\sim |\partial u/\partial x|$.

We first derive H_c and the undulation wavelength $2\pi/q_{xc}$ at H_c. In these calculations, the fourth order term in u in Eq.(18) can be disregarded [4]. We relax the condition $u(z = \pm a/2) = 0$ and solve the Euler-Lagrange equation with boundary conditions following from Eq.(18). This yields the standard solution

$$u(x, z) = u_0 \cos q_z z \sin q_x x \tag{19}$$

with constraints on the wave vectors q_x and q_z:

$$q_z = q_x \sqrt{\kappa - \lambda^2 q_x^2}, \tag{20}$$

$$\frac{B}{W_a} = \frac{q_x \cot\left(\frac{aq_x}{2}\sqrt{\kappa - \lambda^2 q_x^2}\right)}{\sqrt{\kappa - \lambda^2 q_x^2}} \equiv g(q_x), \tag{21}$$

where $\kappa = -\chi_a H^2/B > 0$. The function $g(q_x)$ is even in q_x with two minima. When the ordinate of the two minima is B/W_a, the corresponding

abscissa are $\pm q_{xc}$. Minimization of $g\,(q_x)$ gives the condition $\kappa_c = \lambda^2 a q_{xc}^2/\alpha$, which allows one to find the critical field of undulations in the cell with finite anchoring

$$H_c = q_{xc}\sqrt{\frac{Ka}{\alpha|\chi_a|}} \tag{22}$$

and the relationship between q_{xc} and q_{zc} from (20):

$$q_{xc}^2 = \frac{q_{zc}}{\lambda}\sqrt{\frac{\beta}{\alpha}}. \tag{23}$$

Here $\alpha = \frac{a}{2}\left(1 - \frac{\sin q_{zc}a}{q_{zc}a}\right)$ and $\beta = \frac{a}{2}\left(1 + \frac{\sin q_{zc}a}{q_{zc}a}\right)$. For $W_a \longrightarrow \infty$, Eqs.(21)-(23) recover the results of the classic theory [4, 10], namely, $H_c = \sqrt{\frac{2\pi K}{\lambda a|\chi_a|}}$, $q_{xc}^2 = \frac{\pi}{a\lambda}$, and $q_z = \pi/a$.

In order to calculate the displacement above H_c, we retain the forth order term in Eq.(18). With Eq.(19), the energy density per one period of undulation immediately above the threshold is:

$$\tilde{f} = F\frac{q_x}{2\pi a} = \frac{q_z\chi_a}{4\lambda a}\sqrt{\alpha\beta}\left\{H_c^2 - H^2\right\}u_0^2 + \frac{3Kq_z\alpha\rho}{1024\lambda^4\beta a}u_0^4, \tag{24}$$

where $\rho = 6aq_{zc} + 8\sin q_{zc}a + \sin 2q_{zc}a$. Minimization of Eq.(24) yields the dependence $u_0\,(H)$ above H_c for the case of finite anchoring of layers at the boundaries:

$$u_0 = \frac{8\lambda\eta}{3}\left(\frac{H^2}{H_c^2} - 1\right)^{1/2}; \quad \eta = q_{xc}\left(\frac{6\lambda a}{\rho}\right)^{1/2}\left(\frac{\beta}{\alpha}\right)^{3/4}; \tag{25}$$

H_c is specified by Eq.(22). The last expression (25) for u_0 reduces to the classic result Eq.(17), $\eta = 1$, when $W_a \to \infty$ (as easy to see by calculating ρ, α, and β with $q_{zc} = \pi/a$).

The dependence u_0 on the magnetic field H is of the same square-root character $u_0 \sim (H^2 - H_c^2)^{1/2}$ as in the standard theory. However, the finite value of W_a increases the value of u_0, allowing for larger displacements as compared for the case when $W_a \to \infty$. In addition, finite W_a decreases the value of the threshold field H_c.

The coefficient η in Eq.(25) depends on λ, a and W_a/B through the dependencies of ρ, α, and β on q_{zc},which are the function of W_a/B, see Eqs.(21) and (23). A good fit of the data in Fig.11 is obtained for $\eta = (3.0 \pm 0.5)$ (the only fitting parameter), $\lambda = 2.9$ μm (measured independently in the experiment on dislocations) and $a = 1.7$ mm in Eq.(25).

The fitted values of η corresponds to $W_a/B = (5.2 \pm 0.3)$ μm. The last result leads to the estimate of the anchoring coefficient $W_a = (2.3 \pm 0.1) \times$

$10^{-6}J/m^2$ since in the coarse-grained model $B \approx K_{22}\left(\frac{2\pi}{w}\right)^2 \approx 0.44J/m^3$. The value of W_a agrees in the order of magnitude with a dimensional estimate $W_a \approx K_{22}\left(\frac{2\pi}{w}\right) \approx 10^{-6}J/m^2$ that treats the surface anchoring as the 'intrinsic' anchoring of a lamellar system [17, 18] caused by a violation of layers equidistance near the surface, as discussed in section 2.3. The same estimate $W_a \approx K_{22}\left(\frac{2\pi}{w}\right)$ was found in the studies of cholesteric oily streaks [19]. Note also that the finite W_a calculated above reduces the threshold field H_c, see Eq.(22), by a factor of ≈ 0.8 as compared to its classical value at $W_a \to \infty$ in Eq.(15).

4.4. UNDULATIONS PROFILE WELL ABOVE THE THRESHOLD.

At the onset of undulation, the layers are of a sinusoidal shape, Fig.13a. As the applied field increases above H_c, the wave acquires higher Fourier components and a saw-tooth shape while simultaneously increasing the wavelength, Fig.13b-d. The maximum tilt angle of the layers in the saw-tooth wave grows quickly in the vicinity of H_c and become almost linearly dependent on the field, Fig.14. The amplitude of layer displacement u_0 increases while its z-dependence becomes weaker at high fields. Eventually the displacement field $u(x,z)$ appears to be z-independent in the middle portion of the cell. At the boundaries, the stripes are displaced slightly but remain continuous up to the field of 1T. Above 1T, the layers join the boundary discontinuously and form array of dislocations, Fig.13d.

All the features of the high-field behavior, namely, the change to the saw-tooth profile, increase of the wavelength and increase of the undulation amplitude u_0 have been seen experimentally in various systems. Seul and Wolf [42] used stripe magnetic domains in ferrimagnetic materials and directly observed these phenomena by changing the stripe periodicity. Flament [47] et al. saw the same tendencies in the layered phase of a ferrofluid. Numerical simulation [34] confirmed these observations, too. Singer [48] took into account the higher order (u^4) term in Eq.(18) and constructed a theory that can explain the behavior of $u(x,z)$ near as well as far above H_c.

To explain the weaker z-dependence of the layer displacement field $u(x,y)$ at the field well above H_c, Singer [48] used a single Fourier approximation for the x-dependence: $u(x,z) = \phi(z)\sin q_x x$. With this form of $u(x,z)$, the Euler-Lagrange equation for the energy functional Eq.(18) is

$$\frac{d^2\phi}{dz^2} - \left(\lambda^2 q_x^4 - \kappa q_x^2\right)\phi - \frac{3q_x^4}{16}\phi^4 = 0, \qquad (26)$$

where $\kappa = -\chi_a H^2/B > 0$, as in the previous section. Note that Eq.(26)

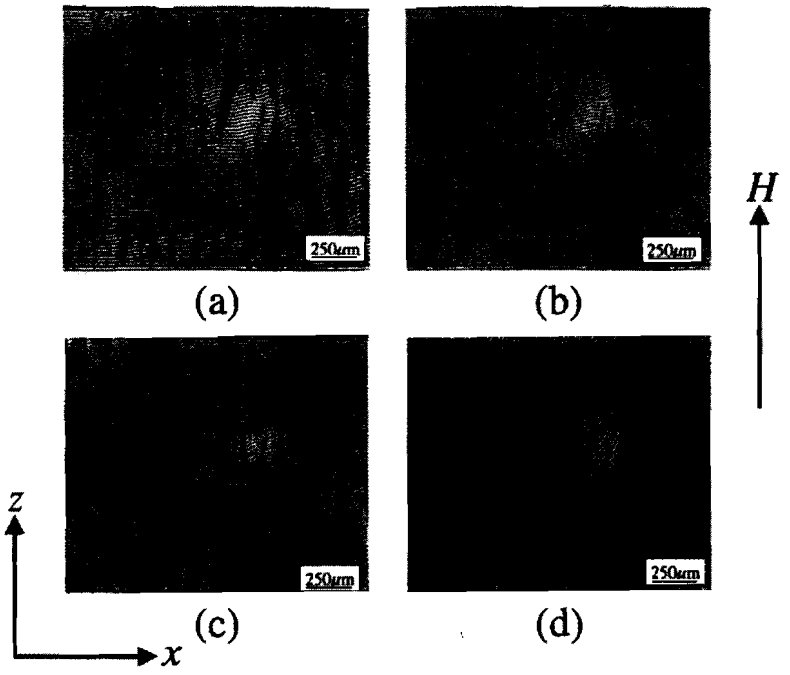

Figure 13. Undulation pattern at different fields. (a) $0.67T$, (b) $0.75T$, (c) $0.81T$ and (d) $1.0T$.

contains a nonlinear term in $\phi(z)$. The solution of Eq.(26) near the threshold is a single Fourier mode profile: $\phi(z) \sim \cos q_z z$. At $H \gg H_c$, however, the profile of $\phi(z)$ flattens out except in the vicinity of the mylar boundaries, see Fig.13b-d. As a result, one can assume that z-dependence of the function $u(x,z)$ is negligible [48]. The experimental data above confirm the validity of this assumption. At high fields, the layers tilt is approximately the same in the middle of the cell and at the bounding plates, since the finite strength of surface anchoring allows for significant tilt at the boundaries. The assumption that the layers profile at high fields becomes eventually z-independent greatly simplifies the analysis and allows us to obtain the layers profile analytically.

First, we explain the field dependence of the tilt angle. Ignoring the z-dependence ($\partial u/\partial z = 0$), one writes the free energy density per unit area in (x,z) plane of the cell as

$$f = \frac{Bl}{2}\left(\frac{1}{4}\theta^4 + \lambda^2\left(\frac{d\theta}{dx}\right)^2 - \kappa\theta^2\right), \tag{27}$$

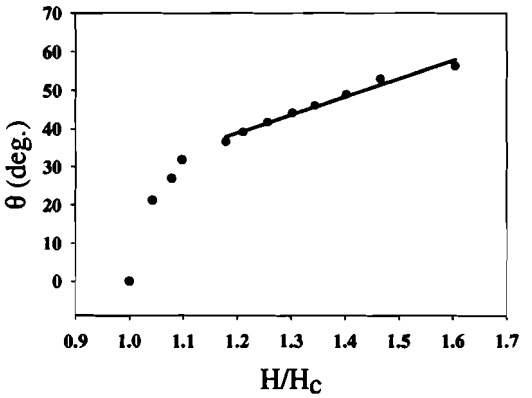

Figure 14. Field dependence of the inclination angle θ of stripes.

where $\theta = \partial u/\partial x$ is the tilt of the layers, and $l \sim P$ is the distance between the glass plates (="thickness" of the pseudo-2D slab). Since $(\partial\theta/\partial x)^2 \geq 0$, the minimum of Eq.(27) is obtained when $\theta = \pm\sqrt{2\kappa} = const.$ The layers produce a saw-tooth (chevron) pattern with alternating $u = \sqrt{2\kappa}x$ and $u = -\sqrt{2\kappa}x$ zones. It also means that the tilt of the layers increases linearly with the field, $\theta \sim |H|$, as observed in the experiment at high fields, Fig.14.

Let us now consider in greater detail the shape of undulating layers in the strong field; experimentally, it appears to be of a saw-tooth type. Singer obtained $u(x)$ in an implicit series form [48].

Below we show that it is possible to directly solve the Euler-Lagrange equation for (27) and to obtain $u(x)$ in a closed form. The Euler-Lagrange equation for the energy density (27) is

$$\lambda^2 \frac{d^2\theta}{dx^2} + \kappa\theta - \theta^3/2 = 0, \tag{28}$$

i.e., equivalent to the equation of motion with a non-linear potential $V(\theta) = -\kappa\theta^2/2 + \theta^4/8$. After some algebra, one obtains a solution in the form $x = x(\theta)$, that is, the horizontal position x in Fig.9 as the function of the layer tilt θ:

$$\frac{x}{2\lambda}\sqrt{4\kappa - \theta_{Max}^2} = \int_0^{\theta/\theta_{Max}} \frac{dt}{\sqrt{(1-t^2)(1-m^2t^2)}}. \tag{29}$$

Here $m^2 = \frac{\theta_{Max}^2}{4\kappa - \theta_{Max}^2} < 1$ and θ_{Max} is the maximum value of θ (as shown above, $\theta_{Max} = \sqrt{2\kappa}$ when there is no z and no x-dependence of the layers

profile). The periodicity L of undulation is given by

$$L = \frac{8\lambda}{\sqrt{4\kappa - \theta_{Max}^2}} K'(m), \tag{30}$$

where $K'(m) = \int_0^1 \frac{dt}{\sqrt{(1-t^2)(1-m^2t^2)}}$ is the complete elliptic integral of the first kind.

Equation (29) expresses x as a function of the tilt θ, whereas inverse expression is more preferable. In order to obtain it, we employ Jacobi's elliptic function. The elliptic integral of the first kind,

$$h = \int^{\omega} \frac{dt}{\sqrt{(1-t^2)(1-m^2t^2)}} \tag{31}$$

is the functional relation between ω and h with a parameter m. When ω is expressed as a function of h, the relationship is specified by one of the Jacobi's elliptic functions,

$$\omega = \mathrm{sn}(h, m). \tag{32}$$

From sn function, we define cn and dn functions [49]:

$$\mathrm{cn}\omega = \sqrt{1 - \mathrm{sn}^2\omega}, \ \mathrm{dn}\omega = \sqrt{1 - m^2\mathrm{sn}^2\omega}. \tag{33}$$

In the limit where $m \to 0$, we have $\mathrm{sn}h \to \sin h$, $\mathrm{cn}h \to \cos h$ and $\mathrm{dn}h \to 1$. Referring to (31) and (32), the spatial behavior of the tilt angle is expressed as

$$\theta(x) = \theta_{Max}\mathrm{sn}\left(\frac{x\sqrt{4\kappa - \theta_{Max}^2}}{2\lambda}, \ m\right). \tag{34}$$

Then layer displacement profile $u(x)$ follows from integration of $\theta(x)$:

$$u(x) = \int^x \theta(x')\,dx' = \theta_{Max} \log\left(-m\mathrm{cn}(x,m) + \mathrm{dn}(x,m)\right) + const. \tag{35}$$

Equation (35) describes an increase in the wavelength, increase in u_0 and change in the shape of undulation pattern towards more pronounced saw-tooth profile when the field-dependent parameter m increases. For small m, the displacement $u(x)$ is sinusoidal. As m becomes large, $u(x)$ exhibits a saw-tooth pattern with a longer periodicity, Fig.15. All these features are in qualitative agreement with the experimentally observed patterns. Note, however, that the radius of curvature at the ridges of the saw-tooth layers becomes smaller as the field increases, approaching the period of the

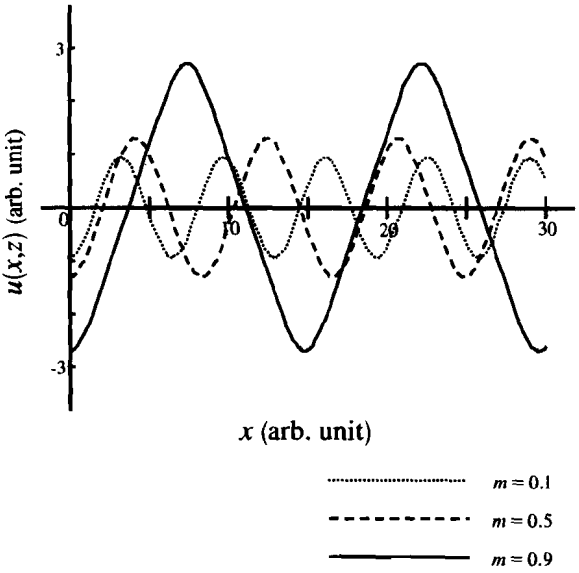

Figure 15. The graph of the function (35) for various values of m.

layered structure itself; therefore, the coarse-grain approximation becomes less justified.

5. Conclusion

We have reviewed our recent studies of the cholesteric "fingerprint" textures that serve as a model of lamellar systems with 1D periodic order. Large (10 microns) periodicity of the cholesteric structures allows for a direct determination of layers configurations through polarizing-microscopy observations.

First, we examined the displacement field of layers around an isolated elementary edge dislocation. Experimental data are well described by a recently suggested nonlinear model of dislocation [8]. In particular, the nonlinear effects manifest themselves in the asymmetry of the dislocation profile. Fitting the experimental data with the non-linear model allows one to determine the penetration length $\lambda = \sqrt{K/B}$ which turns out to be significantly smaller (a factor of 5) than the period of the cholesteric structure. The last feature shows that the cholesteric fingerprint texture is a good examples of a "non-linear" 1D lamellar system in which the elastic free energy density in Eq.(6) should contain the correction term $\left[-\frac{1}{2}\left(\frac{\partial u}{\partial x}\right)^2\right]$.

Second, we used the experimentally determined λ to verify the theoretical predictions for the undulation instability. Undulations were caused by the magnetic field applied normally to the cholesteric stripes. Surprisingly, the amplitude of layers displacements above the threshold field turned out

to be significantly larger than the standard theory predicted. Experimental data suggest that the reason for discrepancies is the finite strength of surface anchoring at the walls that bound the sample. The standard theory assumes that the displacement of layers at the walls is always zero (infinitely strong anchoring). We modified the Helfrich-Hurault theory by accounting for the finite anchoring. The new model, see Eq.(25) and Fig.11, fits the experimental data near the threshold field well and leads to the estimate of the effective layers-related surface anchoring coefficient $W_a \sim K\,(2\pi/P)$, in agreement with the earlier experiments for SmA , Ref. [18] and cholesterics, Ref.[19]. Furthermore, the idea of finite W_a helps to clarify the geometry of undulating layers well above the threshold field. Namely, finite anchoring allows the angular amplitude of layers reorientation in the high field to be practically the same in the center of the cell and near the bounding walls. The analysis of the layers profile at high fields is greatly simplified since one can neglect the dependence of the tilt on the $z-$coordinate perpendicular to the walls. We have found an analytical solutions that describe the essential features of undulations in the high-field regime, namely: the displacement pattern $u\,(x)$ changes from sinusoidal to saw-tooth shape; both the wavelength and amplitude of undulations increase with field, see Eqs.(30)-(35).

We would like to thank M. Kleman and S.V. Shiyanovskii for discussions. The work was supported by NSF Science and Technology Center ALCOM under grant DMR89-21409. Acknowledgment is also made to the donors of the Petroleum Research Fund, administered by the American Chemical Society, for partial support of this research through ACS-PRF grant No. 35306-AC7.

References

1. Landau, L.D. and Lifshitz, E.M., *Course of Theoretical Physics, Statistical Mechanics, Part1,* (Pergamon Press, Oxford, 1980)
2. Chaikin, P.M. and Lubensky, T.C., (1995) *Principles of Condensed Matter Physics.* Cambridge University Press, Cambridge.
3. Holyst, R. (1991) *Phys. Rev. A*, **44**, 3692.
4. Helfrich, W. (1971) *J. Chem. Phys.* **55,** 839; Hurault, J.P. (1973) *J. Chem. Phys.* **59**, 2068.
5. Kleman, M. and Lavrentovich, O.D. (2001) *Soft Matter Physics: An Introduction.* Springer Verlag, New York.
6. Weatherburn, C.E., (1961) *Differential Geometry of Three Dimensions, vol. 1.* Cambridge University Press, Cambridge.
7. Grinstein, G. and Pelcovits, R.A. (1982) *Phys. Rev. A*, **26**, 915.
8. Brener, E.A. and Marchenko, V.I. (1999) *Phys. Rev. E*, **59**, R4752.
9. Nallet, F., Roux, D. and Prost, J., (1989) *Phys. Rev. Lett.* **62**, 276.
10. de Gennes, P.G. and Prost, J., (1992) *Physics of Liquid Crystals,* 2nd ed., Clarendon Press, Oxford.
11. Lubensky, T.C. (1972) *Phys. Rev. A*, **6**, 452.
12. Kats, E.I. and Lebedev, V.V. (1993) *Fluctuational Effects in the Dynamics of Liquid Crystals.* Springer-Verlag, New York, 170pp.

13. Sonin, A.A. (195) *The Surface Physics of Liquid Crystals.* Gordon and Breach Publishers, Luxembourg, 180pp.
14. Quilliet, C., Blanc, C. and Kleman, M. (1996) *Phys. Rev. Lett.*, **77**, 522.
15. Lavrentovich, O.D., Quilliet, C. and Kleman, M.,J. (1997) *Phys. Chem. B*, **101**, 420.
16. Sutton, A.P. and Balluffi, R.W. (1996) *Interfaces in Crystalline Materials.* Oxford Science Publications, Clarendon Press, 820pp.
17. Durand, G. (1993) *Liq. Cryst.*, **14**, 159.
18. Li, Z. and Lavrentovich, O.D. (1994) *Phys. Rev. Lett.*, **73**, 280.
19. Lavrentovich, O.D. and Yang, D.-K. (1998) *Phys. Rev. E*, **57**, R6269.
20. Lavrentovich, O.D. (1986) *Zh. Eksp. Teor. Fiz.*, **91**, 1666 [(1986) *Sov. Phys. JETP*, **64**, 984.]
21. Fournier, J.B. and Durand, G. (1991) *J. Phys. II France*, **1**, 845.
22. Friedel, J. (1964) *Dislocations.* Pergamon press, Oxford.
23. Kleman, M. (1983) *Points, Lines and Walls.* John-Wiley and Sons, New York.
24. Holyst, R. and Oswald, P. (1995) *Int. J. Mod. Phys. B*, **9**, 1515.
25. de Gennes, P.G. (1972) *C. R. Seances Acad. Sci. Ser. B*, **275**, 939.
26. Maaloum, M., Ausserre, D., Chatenay, D., Coulon, G. and Gallot, Y. (1992) *Phys. Rev. Lett.* **68**, 1575.
27. Turner, M. S., Maaloum, M., Ausserre, D., Joanny, J-F. and Kunz, M. (1994) *J. Phys. II France*, **4**, 689.
28. We thank M. Kleman for the illuminating consultations on the available results about the dislocation structures. See also reference [31] for the discussion of dislocation in materials with small and large rigidity.
29. Ishikawa, T. and Lavrentovich, O.D. (1999) *Phys. Rev. E*, **60**, R5037.
30. Subacius, D., Shiyanovskii, S.V., Bos, P. and Lavrentovich, O.D. (1997) *Appl. Phys. Lett.* **71**, 3323.
31. Kleman, M. (1988) *Liq. Cryst.*, **3**, 1355.
32. Williams, C.E. and Kleman, M. (1974) *J. Phys. Lett. France*, **35**, L33.
33. Clark, N.A. and Meyer, R.B (1973) *Appl. Phys. Lett.*, **22**, 493.
34. Fukuda, J. and Onuki, A. (1995) *J. Phys. II France*, **5**, 1107.
35. Ribotta, R. and Durand, G. (1977) *J. Physique*, **38**, 179.
36. Eq.17 is often written with a coefficient $4\sqrt{2}$ instead of 8; we found the coefficient 8 to be correct.
37. Delaye, M., Ribotta, R. and Durand, G. (1973) *Phys. Lett. A*, **44**, 139.
38. Rondelez, F. (1971) *C.R. Acad. Sci. B*, **273**, 549.
39. Moncton, D. E., Pindak, R., Davey, S.C. and Brown, G. (1982) *S., Phys. Rev. Lett.*, **49**, 1865.
40. Gharbia, M., Cagnon, M. and Durand, G. (1985) *J. Phys.Lett. France*, **46**, L683.
41. Molho, P., Porteseil, J.L., Souche, Y., Gouzerh, J. and Levy, J.C.S. (1987) *Appl. Phys. Lett.*, **61**, 4188.
42. Seul, M. and Wolfe, R. (1992) *Phys. Rev. A*,**46**, 7519; (1992) *Phys. Rev. Lett.*, **68**, 2460; (1992) *Phys. Rev. E*, **46**, 7519 and 7534.
43. Elias, F., Flament, C., Bacri, J.-C. and Neveu, S. (1997) *J. Phys. I France*, **7**, 711.
44. Wang, Z.G. (1994) *J. Chem. Phys.*, **100**, 2298.
45. Cohen, Y., Albalak, R.J., Dair, B.J., Capel, M.S. and Thomas, E.L. (2000) *Macromolecules*, **33**, 6502.
46. Ishikawa, T. and Lavrentovich, O.D., Technical Reports **10** 169pp, ALCOM Symposium *Chiral Materials and Applications*, February 18-19, 1999; (2001) *Phys. Rev. E*, **63**, 030501 (R).
47. Flament, C., Bacri, J.C., Cebers, A., Elias, F. and Perzynski, R. (1996) *Europhys Lett.*, **34**, 225.
48. Singer, S.J. (1993) *Phys. Rev. E*, **48**, 2796.
49. Abramowitz, M. and Stegun, I.A. (1965) *Handbook of Mathematical Functions.* Dover, New York.